Factors Governing the Secondary Bjerknes Force Between Ultrasonically Excited Bubbles

X. Wang*, H. Li, Y. Li and C. Zhao

School of Automobile Engineering, Beijing Polytechnic University, Beijing 100176, China

Received: 31.07.2025 & Accepted: 11.12.2025

Doi: 10.12693/APhysPolA.149.3 *e-mail: wxj3282@126.com

Studying the governing parameters and mechanistic principles underlying ultrasound-induced inter-bubble interactions can provide a critical theoretical foundation for advancing engineering applications: coalescence control of bubbles, optimization of cavitation field distributions, and reconfiguration of acoustic energy radiation patterns. This study investigates the governing factors of the secondary Bjerknes force acting between ultrasonically excited bubbles and its manifestations. The results demonstrate that dynamic modifications of the secondary Bjerknes force systematically depend on both ultrasonic excitation parameters and bubble conditions. Within the R_{10}–R_{20} parameter space, this force distribution is divided into four distinct regions according to the linear resonance radius of bubbles. Critically, inter-bubble distance exhibits no significant correlation with the spatial patterning of force distribution. The magnitude of the secondary Bjerknes force increases positively with both decreasing inter-bubble separation and increasing ultrasonic pressure amplitudes. Furthermore, all bubble pairs universally undergo two sign inversions as ultrasonic frequency increases.

topics: ultrasonic excitation, cavitation bubble, secondary Bjerknes force, sign inversion

1. Introduction

Ultrasonic cavitation causes the microbubble nucleation, nonlinear oscillation, and inertial collapse in liquids under ultrasound exposure. The generated extreme mechanochemical effects (shock waves > 1 GPa, microjets > 100 m/s) can facilitate industrial processes and medical therapies [1–9]. Bubbles typically form clusters within acoustic fields. The inter-bubble coupling triggered by bubble-induced pressure waves is predominantly described by secondary Bjerknes forces. These forces drive multi-scale self-organization of bubbles, leading to complex bubble cloud morphologies — a structural evolution that critically determines energy distribution patterns in ultrasonic fields [10–12].

The theoretical underpinning of the Bjerknes forces was first formalized by Bjerknes [13]. Crum et al. [14] pioneered the experimental measurement of the secondary Bjerknes force in a low-pressure acoustic field and derived its mathematical expression under the assumption of spherical bubble oscillations. Subsequently, Mettin et al. [15] extended this work and developed a model to describe the interaction under nonlinear oscillations in a high-intensity ultrasonic field. Building upon this framework, numerous researchers conducted theoretical investigations into the secondary Bjerknes force. Zhang et al. [16] found that liquid compressibility serves as a critical parameter determining both the direction and magnitude of the secondary Bjerknes force. Other scholars investigated the influences of pressure amplitude, physical parameters, distance between the bubbles, and equilibrium radii of bubble pairs on the secondary Bjerknes force [17–20]. The effect of surface waves on the secondary Bjerknes force in a microfluidic channel was also considered [21]. Additionally, Zhang studied the secondary Bjerknes force under dual-frequency ultrasound [22]. Chen et al. [23] then analyzed this force in a three-bubble system. They found that the modulation effects strongly depend on bubble size, with enhanced effects occurring when the third bubble was near the smaller bubble in the pair. Wang et al. [24] further investigated the dynamic behaviors and the secondary Bjerknes force in multi-bubble systems, explaining several key phenomena in bubble clusters.

Ultrasonic cavitation engineering is fundamentally governed by bubble dynamics behavior, which is largely regulated by inter-bubble interactions [25–28]. Fan et al. [29] conducted a systematic investigation on how cell cycle phases affect drug

delivery efficiency during multi-bubble sonoporation. Meng et al. [30] developed a microfluidic platform system that utilizes secondary radiation forces to immobilize individual cells at microbubble interfaces. Qin et al. [31] studied how bubble interactions affect acoustic cavitation in a two-bubble system and showed that these effects strongly depend on ultrasound parameters, bubble properties, and the surrounding liquid.

While substantial understanding of secondary Bjerknes forces has been achieved via theoretical and experimental investigations, universal conclusions quantifying the control parameters of these forces have yet to be established. Given the critical role of bubble–bubble interaction forces in bubble dynamics, this work will systematically analyze key variables governing the interaction dynamics and their quantitative relationships. Specifically, the theoretical framework governing secondary Bjerknes forces is presented in Sect. 2, followed by results and their corresponding discussion through Sect. 3. Conclusive insights are consolidated in Sect. 4. The complete implementation code utilized in this work has been made publicly available via GitHub [32]. Furthermore, the code is also provided in the Appendix.

2. Numerical model

Our dual-bubble model (designated bubble 1 and bubble 2) operates under the following assumptions: (i) ultrasonic wavelengths exceed bubble dimensions and inter-bubble distances, ensuring spherical oscillation symmetry; (ii) isothermal conditions are throughout (thermal contributions from oscillating bubbles are negligible); and (iii) the liquid surrounding the bubble is incompressible and irrotational [15, 33, 34]. Due to the coupling effect among the bubbles, their oscillations exhibit an interactive rather than independent behavior.

Bubble 1's radial oscillations generate a spherically symmetric velocity field in the surrounding liquid, described by

$$u_1 = \frac{R_1^2 \dot{R}_1}{r_1^2}, \tag{1}$$

where u_1 is the spherically symmetric liquid velocity field generated by bubble 1's radial oscillations, r_1 denotes the distance from bubble 1's center to an arbitrary field point, and $\dot{R}_1$ represents bubble 1's radial oscillation velocity.

The governing flow equation is employed to compute the pressure distribution induced by bubble 1's radial oscillations

$$\rho \frac{\partial u_1}{\partial t} + \frac{\partial p_{s1}}{\partial r} = 0, \tag{2}$$

where p_{s1} denotes the scattered pressure generated by bubble 1's radial oscillation.

Subsequent substitution of (1) into (2) and integration yields the pressure gradient field induced by bubble 1's oscillation

$$\frac{\partial p_{s1}}{\partial r} = -\frac{\rho}{r^2}\frac{\mathrm{d}}{\mathrm{d}t}\big(R_1^2 \dot{R}_1\big), \tag{3}$$

$$p_{s1} = \frac{\rho}{r}\frac{\mathrm{d}}{\mathrm{d}t}\big(R_1^2 \dot{R}_1\big), \tag{4}$$

where ρ is the liquid density.

The radial oscillation of bubble 1 establishes a pressure gradient field ∇p_{s1} within the surrounding fluid. Consequently, the radiation pressure acting from bubble 1 to bubble 2 is given by

$$F_{12} = -V_2 \nabla p_{s1}, \tag{5}$$

where V_2 denotes the volume of bubble 2, and $V_2 = 4\pi R_2^3/3$. Substitution of (4) into (5) yields

$$F_{12} = -V_2 \frac{\partial p_{s1}}{\partial D} = V_2 \frac{\rho}{D^2}\frac{\mathrm{d}\big(R_1^2 \dot{R}_1\big)}{\mathrm{d}t} = \frac{\rho V_2}{4\pi D^2}\frac{\mathrm{d}^2 V_1}{\mathrm{d}t^2}, \tag{6}$$

where D represents the time-varying distance between the centers of bubble 1 and bubble 2. With bubble 1 volume V_1 (where $V_1 = 4\pi R_1^3/3$), $\ddot{V}_1$ expresses its volumetric acceleration.

Integrating (6) over an acoustic cycle yields the secondary Bjerknes force F_B exerted by bubble 1's radial oscillation on bubble 2

$$F_B = \langle F_{12} \rangle = -\frac{\rho}{4\pi D^2}\left\langle \dot{V}_1 \dot{V}_2 \right\rangle, \tag{7}$$

where $\dot{V}_1$ and $\dot{V}_2$ are volumetric change rates of bubble 1 and bubble 2 (respectively, $\dot{V}_1 = 4\pi R_1^2 \dot{R}_1$, $\dot{V}_2 = 4\pi R_2^2 \dot{R}_2$); $\langle \cdot \rangle$ denotes the time average during one oscillation period.

The identical methodology allows us to derive the secondary Bjerknes force exerted by bubble 2 on bubble 1. Under the instantaneous interaction approximation (negligible inter-bubble time delay), the force magnitudes are identical with antiparallel directions, $\langle F_{12} \rangle = -\langle F_{21} \rangle$.

We employ Doinikov's coupled nonlinear model [35] describing bubble interactions. Bubbles 1 and 2 exhibit strongly coupled dynamics, with their radial pulsations and translational movements directly affecting each other

$$\begin{aligned}
&\Big(1-\frac{\dot{R}_1}{c}\Big)R_1\ddot{R}_1 + \dot{R}_1^2\Big(\frac{3}{2}-\frac{\dot{R}_1}{2c}\Big) - \frac{P_1}{\rho}\Big(1+\frac{\dot{R}_1}{c}\Big) \\
&\quad - \frac{R_1}{\rho c}\frac{\mathrm{d}P_1}{\mathrm{d}t} = \frac{\dot{x}_1^2}{4} - \frac{R_2\ddot{R}_2 + 2R_2\dot{R}_2^2}{D} \\
&\quad + \frac{R_2^2(\dot{x}_1\dot{R}_2 + R_2\ddot{x}_2 + 5\dot{R}_2\dot{x}_2)}{2D^2} - \frac{R_2^3\dot{x}_2(\dot{x}_1+2\dot{x}_2)}{2D^3},
\end{aligned} \tag{8}$$

$$\begin{aligned}
&\Big(1-\frac{\dot{R}_2}{c}\Big)R_2\ddot{R}_2 + \dot{R}_2^2\Big(\frac{3}{2}-\frac{\dot{R}_2}{2c}\Big) - \frac{P_2}{\rho}\Big(1+\frac{\dot{R}_2}{c}\Big) \\
&\quad - \frac{R_2}{\rho c}\frac{\mathrm{d}P_2}{\mathrm{d}t} = \frac{\dot{x}_2^2}{4} - \frac{R_1^2\ddot{R}_1 + 2R_1\dot{R}_1^2}{D} \\
&\quad - \frac{R_1^2(\dot{x}_2\dot{R}_1 + R_1\ddot{x}_1 + 5\dot{R}_1\dot{x}_1)}{2D^2} - \frac{R_1^3\dot{x}_1(\dot{x}_2+2\dot{x}_1)}{2D^3},
\end{aligned} \tag{9}$$

$$\frac{R_1\ddot{x}_1}{3}+\dot{R}_1\dot{x}_1+\frac{1}{D^2}\frac{\mathrm{d}}{\mathrm{d}t}\Big(R_1R_2^2\dot{R}_2\Big) - \frac{R_2^2(R_1R_2\ddot{x}_2+R_2\dot{R}_1\dot{x}_2+5R_1\dot{R}_2\dot{x}_2)}{D^3}=\frac{F_{ex1}}{2\pi\rho R_1^2}, \tag{10}$$

$$\frac{R_2\ddot{x}_2}{3}+\dot{R}_2\dot{x}_2-\frac{1}{D^2}\frac{\mathrm{d}}{\mathrm{d}t}(R_2R_1^2\dot{R}_1) - \frac{R_1^2(R_2R_1\ddot{x}_1+R_1\dot{R}_2\dot{x}_1+5R_2\dot{R}_1\dot{x}_1)}{D^3}=\frac{F_{ex2}}{2\pi\rho R_2^2}. \tag{11}$$

Here, $\ddot{R}_1$ and $\ddot{R}_2$ denote the radial accelerations of the bubbles, x_1 and x_2 are the positions of bubbles 1 and 2, respectively, $\dot{x}_1$ and $\dot{x}_2$ represent their translational velocities, and $\ddot{x}_1$ and $\ddot{x}_2$ are their translational accelerations.

The surface pressures acting on bubbles 1 and 2 are denoted P_1 and P_2, where

$$P_1=\Big(P_0-P_v+\frac{2\sigma}{R_{10}}\Big)\left(\frac{R_{10}}{R_1}\right)^{3\kappa}+P_v-\frac{2\sigma}{R_1}-\frac{4\mu\dot{R}_1}{R_1} -P_0-P_d(t), \tag{12}$$

$$P_2=\Big(P_0-P_v+\frac{2\sigma}{R_{20}}\Big)\left(\frac{R_{20}}{R_2}\right)^{3\kappa}+P_v-\frac{2\sigma}{R_2}-\frac{4\mu\dot{R}_2}{R_2} -P_0-P_d(t). \tag{13}$$

The above parameters include fluid properties (c — sound velocity, μ — viscosity), interfacial parameter (σ — surface tension), thermodynamic constant (κ — polytropic exponent), and environmental terms (P_v — vapor pressure, P_0 — atmospheric static pressure). The acoustic excitation is described by $P_d(t)$

$$P_d\left(t\right)=-P_a\sin\left(2\pi f_0 t\right), \tag{14}$$

where P_a denotes the ultrasonic pressure, and f_0 represents the ultrasonic frequency.

The dominant external forces acting on the bubbles are modeled by Levich's viscous drag force formulation [36]

$$F_{ex1}=-12\pi\mu R_1(\dot{x}_1-\nu_2), \tag{15}$$

$$F_{ex2}=-12\pi\mu R_2(\dot{x}_2-\nu_1), \tag{16}$$

where v_1 and v_2 are the liquid velocities generated by bubbles 1 and 2, respectively,

$$\nu_1=\frac{R_1^2\dot{R}_1}{D^2}+\frac{R_1^3\dot{x}_1}{D^3}, \tag{17}$$

$$\nu_2=-\frac{R_2^2\dot{R}_2}{D^2}+\frac{R_2^3\dot{x}_2}{D^3}. \tag{18}$$

The governing equations (see (8)–(11)) are integrated numerically using a 4(5)-order Runge–Kutta–Fehlberg algorithm with an adaptive time-stepping. The fixed parameters are: $\mu=0.001$ (Pa s), $\sigma=0.0728$ N/m, $c=1500$ m/s, $\kappa=4/3$, $\rho=998$ kg/m^3, $P_v=2330$ kPa, and $P_0=100$ kPa.

For an isolated bubble in an infinite liquid domain (inter-bubble coupling is negligible), the linear resonance frequency is given by [37]

$$f_{res}=\frac{1}{2\pi R_0\sqrt{\rho}}\sqrt{3\kappa\left(P_0+\frac{2\sigma}{R_0}-P_v\right)-\frac{2\sigma}{R_0}-\frac{4\mu^2}{\rho R_0^2}}. \tag{19}$$

3. Results and discussion

The secondary Bjerknes force originates from the second sound field produced by the radial oscillations of the bubble itself [38]. The bubble dynamics are influenced by its initial radius, the inter-bubble distance, and the ultrasonic excitation parameter, all of which, in turn, affect the secondary Bjerknes force. This section investigates how these factors influence the secondary Bjerknes force.

3.1. The effects of initial bubble radius and inter-bubble distance on F_B

3.1.1. Initial bubble radius

Figure 1 illustrates the time-varying secondary Bjerknes force (F_B) as a function of the number of ultrasonic excitation periods (N) for bubbles with initial radii of 15, 25, 35, and 45 μm. In ultrasonic systems, the excitation period is defined as the duration of one complete oscillation period of the acoustic source (sinusoidal waveform). The ultrasound pressure amplitude P_a is 10 kPa, the frequency f_0 is 100 kHz, and the inter-bubble distance D_0 is 1000 μm.

As shown in Fig. 1, F_B is attractive across all cases considered. The absolute value of F_B initially increases and then decreases as the initial bubble radius (R_{10} or R_{20}) increases, reaching its maximum value at R_{10} (or R_{20}) $= 35$ μm. At the ultrasonic frequency (f_0) of 100 kHz, the bubble's linear resonance radius (R_{res}) is $\approx$ 34 μm. This indicates that the observed non-monotonic variation in the absolute value of F_B (its increase followed by a decrease) is driven by variations in the initial bubble radius as it approaches the resonance radius. Additionally, temporal inconsistencies in F_B oscillations emerge within individual ultrasound excitation periods, particularly for bubble pairs with an initial radius of 15 μm. For bubbles with an initial radius of 35 μm, the magnitude of F_B exhibits a decline with increasing excitation cycles (N). This behavior occurs as the initial bubble radii approach the resonance radius. This proximity amplifies F_B, which subsequently enhances suppression of radial bubble oscillations, ultimately reducing the absolute value of F_B.

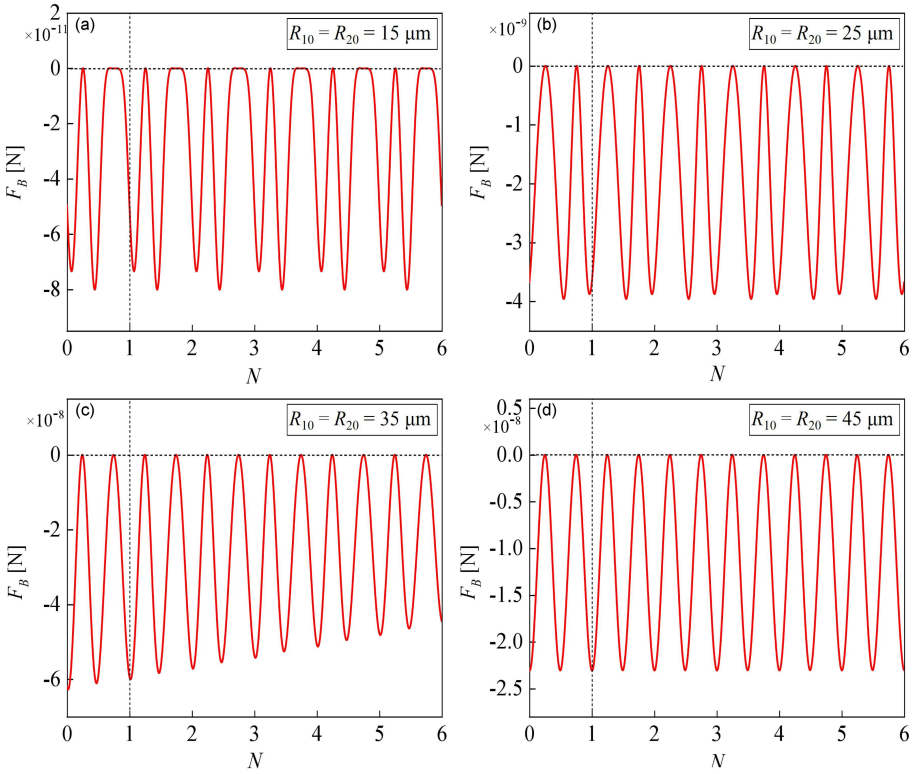

Fig. 1. Variations of the secondary Bjerknes force (F_B) with the number of ultrasonic excitation periods (N) for bubbles with the same initial radii. Here, (a) $R_{10} = R_{20} = 15$ μm; (b) $R_{10} = R_{20} = 25$ μm; (c) $R_{10} = R_{20} = 35$ μm; (d) $R_{10} = R_{20} = 45$ μm. In all cases (a–d), $P_a = 10$ kPa, $f_0 = 100$ kHz, and $D_0 = 1000$ μm.

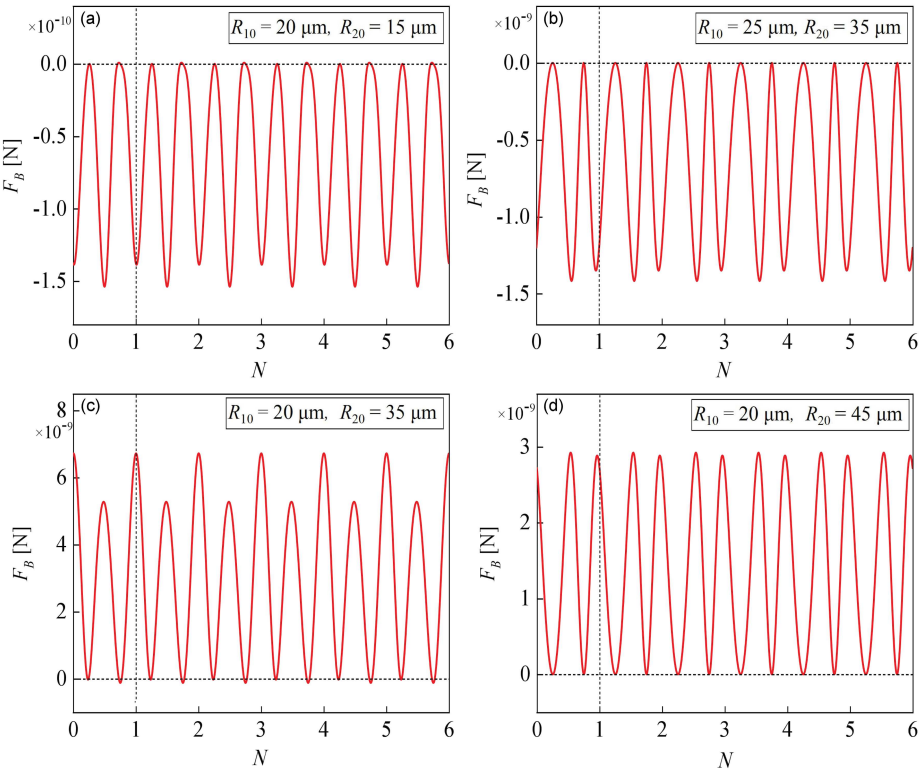

Fig. 2. Variations of F_B with the number of ultrasonic excitation periods (N) for bubbles with different initial radii. Here, (a) $R_{10} = 20$ μm, $R_{20} = 15$ μm; (b) $R_{10} = 20$ μm, $R_{20} = 25$ μm; (c) $R_{10} = 20$ μm, $R_{20} = 35$ μm; (d) $R_{10} = 20$ μm, $R_{20} = 45$ μm. In all cases (a–d), $P_a = 10$ kPa, $f_0 = 100$ kHz, and $D_0 = 1000$ μm.

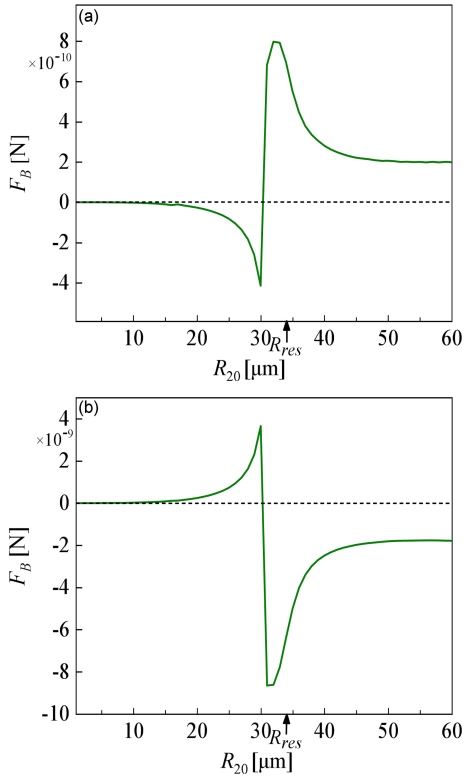

Fig. 3. Variations of F_B with initial radius of bubble 2 (R_{20}) at fixed initial radius of bubble 1 (R_{10}). Here, (a) $R_{10} = 10$ μm; (b) $R_{10} = 50$ μm. In all cases (a–b), $P_a = 10$ kPa, $f_0 = 100$ kHz, and $D_0 = 1000$ μm.

Figure 2 illustrates the variation of the time-varying secondary Bjerknes force (F_B) across the number of ultrasonic excitation periods (N) for bubble pairs with different initial radii. In all cases, a constant initial radius $R_{10} = 20$ μm is maintained. The behavior of F_B exhibits clear trends governed by the relationship between R_{20} and the resonance radius R_{res} (≈ 34 μm). When R_{20} is smaller than R_{res}, F_B acts attractively; when R_{20} exceeds R_{res}, F_B becomes repulsive. Among the four configurations, the magnitude of F_B peaks when R_{20} approaches R_{res}.

To better visualize how F_B varies with the bubble initial radius, in Fig. 3 we show the time-averaged F_B varying with R_{20} at fixed R_{10}. The data show that F_B reverses sign depending on the bubble sizes and relative to R_{res}.

As shown in Fig. 3a, when $R_{20} < R_{res}$, F_B increases steadily as R_{20} increases. However, F_B abruptly reverses sign from positive to negative near R_{res}. Beyond R_{res}, the repulsive force decreases steadily. In Fig. 3b, when $R_{20} > R_{res}$, F_B increases with R_{20} but undergoes a sharp reversal near R_{res}, shifting from repulsive to attractive. Beyond this point, F_B weakens as R_{20} increases further. In both cases, F_B reaches its maximum magnitude near R_{res}.

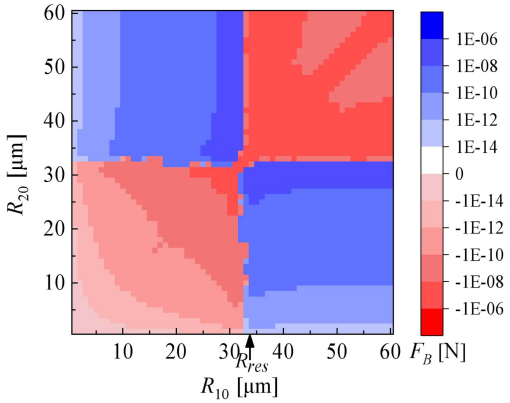

Fig. 4. Distributions of the secondary Bjerknes force (F_B) in the R_{10}–R_{20} plane, where $P_a = 10$ kPa, $f_0 = 100$ kHz, and $D_0 = 1000$ μm.

Figure 4 shows the distribution of F_B in the R_{10}–R_{20} plane, where R_{10} and R_{20} are variables. The secondary Bjerknes force is represented as the time-averaged force over one ultrasonic excitation period. The red regions ($F_B < 0$) correspond to attractive forces, while blue regions ($F_B > 0$) represent repulsive forces.

In Fig. 4, it can be seen that F_B is symmetrically distributed in the R_{10}–R_{20} plane along the diagonal line. Using the linear resonance radius points of the two bubbles as boundaries, the distribution of F_B can be divided into four distinct regions. Specifically, attractive forces occur when either (i) $R_{10} < R_{res}$ and $R_{20} < R_{res}$ or (ii) $R_{10} > R_{res}$ and $R_{20} > R_{res}$. Conversely, repulsive forces occur when (i) $R_{10} < R_{res}$ and $R_{20} > R_{res}$ or (ii) $R_{10} > R_{res}$ and $R_{20} < R_{res}$. Along the diagonal of the R_{10}–R_{20} plane, F_B consistently shows positive values, indicating that F_B is always attractive when R_{10} and R_{20} are nearly equal. Additionally, the peak magnitude of F_B is observed when both initial radii approach R_{res}. Furthermore, F_B intensifies significantly when either R_{10} or R_{20} nears R_{res}, showing notably higher values than elsewhere in the plane.

3.1.2. Inter-bubble distance

Figure 5 illustrates the variations of the secondary Bjerknes force (F_B) with the number of excitation periods (N) at different inter-bubble distances (D_0). The ultrasound pressure (P_a) is 10 kPa, and the frequency (f_0) is 100 kHz. Crucially, D_0 influences only the magnitude of F_B, regardless of whether the initial radii (R_{10} and R_{20}) are equal or unequal. The magnitude of F_B increases as D_0 decreases, with the growth rate accelerating at smaller D_0.

In Fig.6 we examine the variations in F_B with R_{20} at different D_0, when R_{10} is held constant. Results represent time-averaged F_B over a single

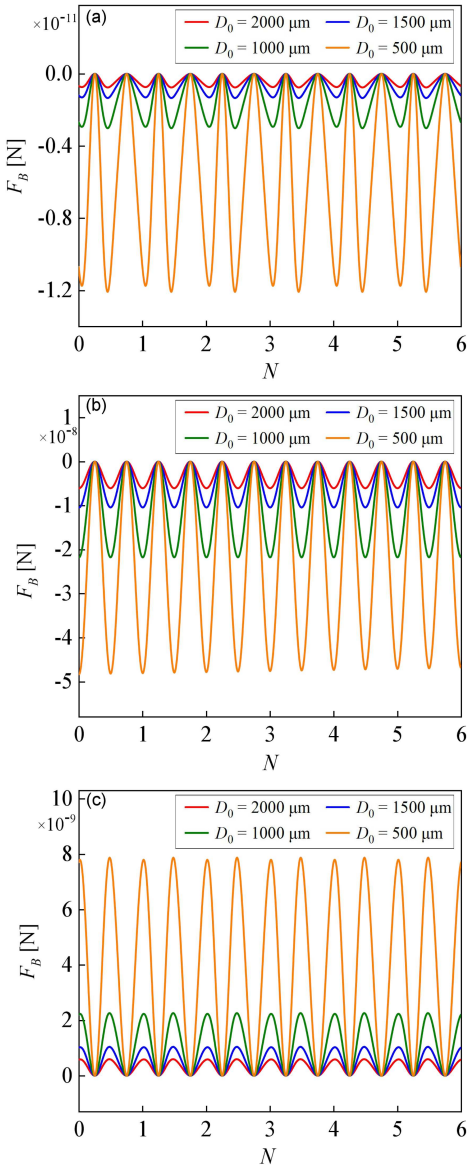

Fig. 5. Variations of F_B with the number of ultrasonic excitation periods (N) at different inter-bubble distances (D_0). Here, (a) $R_{10} = R_{20} = 10$ μm; (b) $R_{10} = R_{20} = 50$ μm; (c) $R_{10} = 10$ μm, $R_{20} = 50$ μm. In all cases (a–c), $P_a = 10$ kPa and $f_0 = 100$ kHz.

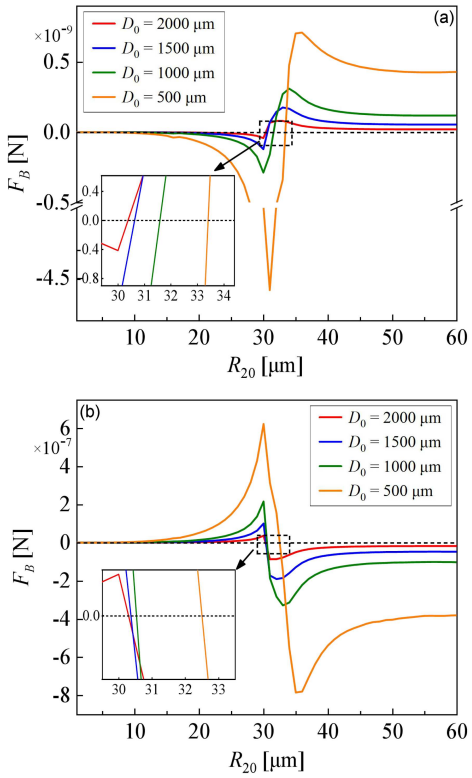

Fig. 6. Variations of F_B with initial radius of bubble 2 (R_{20}) at different inter-bubble distances (D_0). Here, (a) $R_{10} = 10$ μm; (b) $R_{10} = 50$ μm. In all cases (a–b), $P_a = 10$ kPa, $f_0 = 100$ kHz.

ultrasonic excitation period. It is clear that regardless of whether R_{10} is smaller or larger than the linear resonance radius (R_{res}), the influence of D_0 on F_B is the strongest when R_{20} approaches R_{res}. Additionally, the value of R_{20} at which F_B changes direction (i.e., transitioning from attractive to repulsive force or vice versa) consistently lies slightly below R_{res}, converging toward R_{res} with decreasing D_0.

Figure 7 illustrates the distribution of time-averaged F_B in the R_{10}–R_{20} plane for $D_0 = 2000$, 1500, 1000, and 500 μm. As can be seen, the distribution patterns of F_B in the R_{10}–R_{20} plane remain consistent across different D_0. The magnitude of F_B increases as D_0 decreases, particularly when R_{10} (or R_{20}) approaches R_{res}. Furthermore, as D_0 decreases, R_{res} increases due to inter-bubble coupling effects. Consequently, the boundary separating attractive and repulsive regimes shifts toward larger initial radii, correspondingly altering their phase-space areas.

3.2. The effects of ultrasonic excitation parameters on F_B

3.2.1. Ultrasonic pressure amplitude

Ultrasonic pressure influences the secondary Bjerknes force by dominantly governing bubble radial oscillation. Figure 8 illustrates the variation of the secondary Bjerknes force (F_B) as a function of the number of ultrasonic excitation cycles (N) for bubbles with the same initial radii of 15 μm at different ultrasonic pressure amplitudes (P_a). The ultrasonic frequency (f_0) is set as 100 kHz, and the inter-bubble distance (D_0) is 1000 μm. It can be observed that the absolute value of F_B increases as P_a increases, which is due to the intensified bubble radial oscillations at higher P_a. Furthermore, P_a influences both the magnitude of F_B and its variation

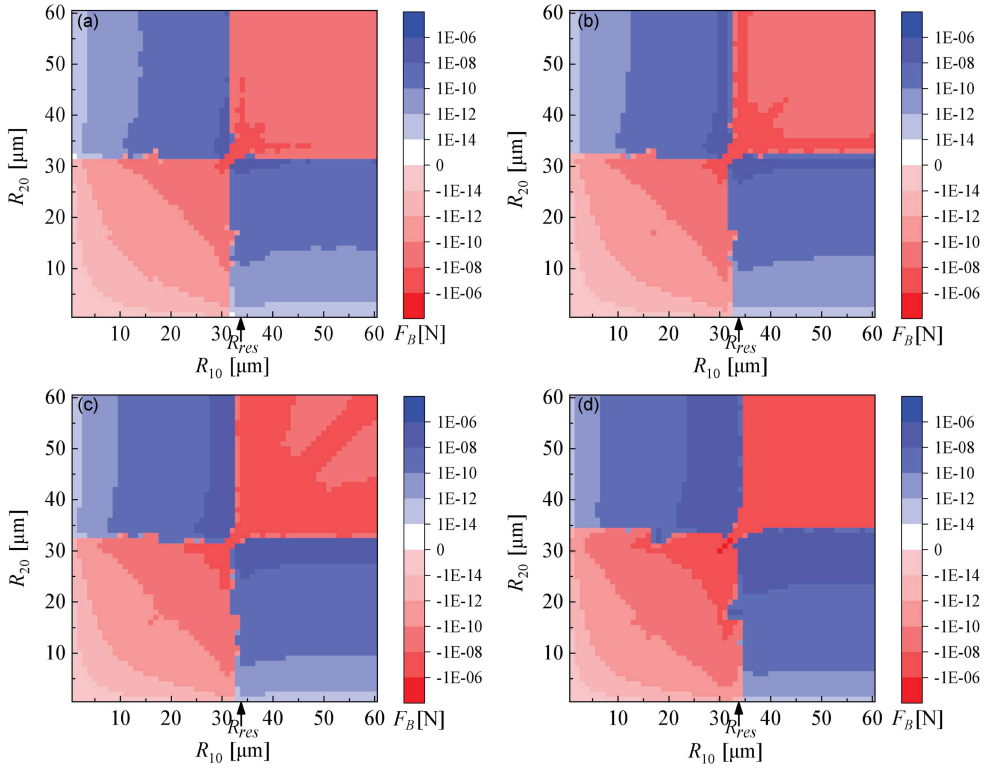

Fig. 7. Distributions of F_B in the R_{10}–R_{20} plane at different inter-bubble distances (D_0). Here, (a) $D_0 = 2000$ μm; (b) $D_0 = 1500$ μm; (c) $D_0 = 1000$ μm; (d) $D_0 = 500$ μm. In all cases (a–d), $P_a = 10$ kPa and $f_0 = 100$ kHz.

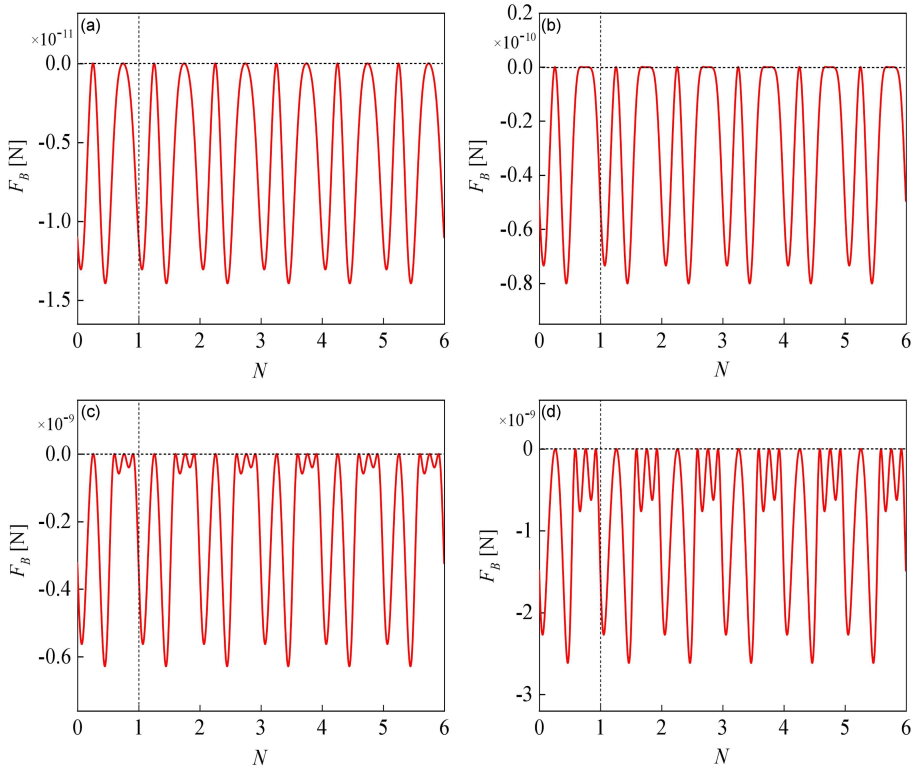

Fig. 8. Variations of F_B with the number of ultrasonic excitation periods (N) for bubbles with the same radii at different ultrasonic pressure amplitudes (P_a). Here, (a) $P_a = 5$ kPa; (b) $P_a = 10$ kPa; (c) $P_a = 20$ kPa; (d) $P_a = 30$ kPa. In all cases (a–d), $f_0 = 100$ kHz and $D_0 = 1000$ μm.

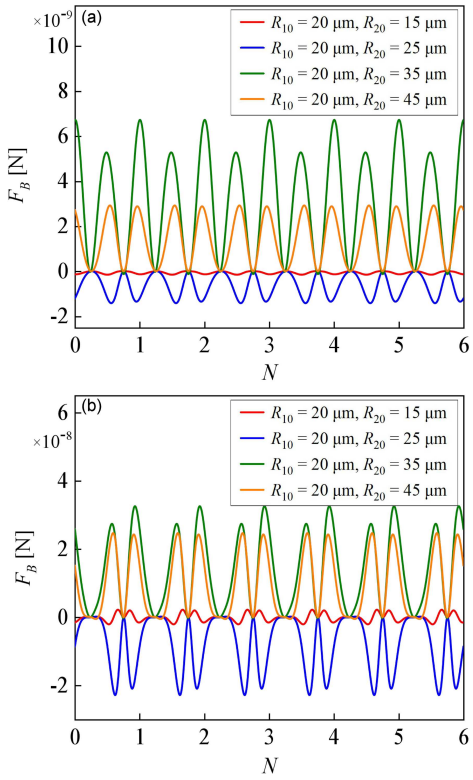

Fig. 9. Variations of F_B with the number of ultrasonic excitation periods (N) for bubbles with different radii at different ultrasonic pressure amplitudes (P_a). Here, (a) $P_a = 10$ kPa; (b) $P_a = 30$ kPa. In all cases (a–b), $f_0 = 100$ kHz and $D_0 = 1000$ μm.

characteristics. As P_a increases, the difference between the dual-oscillation peaks of F_B within a single cycle becomes more pronounced.

Figure 9 shows the variation of F_B with N for bubbles with different radii under varying P_a. It is revealed that at higher P_a, the absolute value of F_B exhibits significantly larger magnitudes when initial bubble radii (R_{10} and R_{20}) differ, and the magnitude enhancement varies across bubble pairs. Furthermore, P_a influences both the magnitude of F_B and its variation characteristics, consistent with behavior observed in bubbles with identical initial radii. Research indicates that elevated P_a amplifies the main resonance intensity while concurrently enhancing subharmonic and harmonic resonances. These intensified resonances exert progressively stronger influence on bubble radial oscillations, thereby dominantly governing the variation characteristics of F_B. Specifically, for bubbles with initial radii $R_{10} = 20$ μm and $R_{20} = 15$ μm, F_B predominantly acts as an attractive force at $P_a = 10$ kPa. At the elevated pressure of $P_a = 30$ kPa, F_B periodically reverses direction, oscillating distinctly between attraction and repulsion. This transition is linked to strengthened harmonic resonances, providing a plausible explanation for the observed behavior.

Figure 10 illustrates the variation of F_B as a function of P_a for bubble pairs of different initial radii. Among these bubble pairs, F_B exhibits distinct behaviors as P_a increases. As depicted in Fig. 10b–d, the magnitude of F_B exhibits a monotonic increase with rising P_a. However, for the bubble pair with $R_{10} = 20$ μm and $R_{20} = 15$ μm (Fig. 10a), F_B exhibits non-monotonic behavior, initially increasing and then decreasing with rising P_a. This behavior stems from the proximity of their initial radii to the 2nd-order harmonic resonance radius ($0.5R_{res} \approx 17$ μm), calculated via (19). Such proximity activates pronounced 2nd-order harmonic resonance effects, consequently reversing F_B.

In Fig. 11, we present the distribution of time-averaged F_B in the R_{10}–R_{20} plane under varying P_a. The secondary Bjerknes force reversal occurs both when R_{10} and/or R_{20} approach R_{res} (i.e., $R_{res} \approx 34$ μm) and when they approach the 2nd-order harmonic resonance radius (i.e., $0.5R_{res} \approx 17$ μm) at elevated P_a (see Fig. 11c and d). Additionally, R_{res} decreases with increasing P_a due to inter-bubble interactions. This shifts the attractive/repulsive boundary toward smaller initial radii, consequently altering the areas of the four regions in the plane.

3.2.2. Ultrasonic frequency

Ultrasonic frequency (f_0) influences the secondary Bjerknes force between bubbles by modifying their radial oscillations. Figure 12 shows the variation of time-varying F_B with the number of ultrasonic excitation periods (N) at different f_0. For equal initial radii ($R_{10} = R_{20}$), F_B increases with f_0. Comparison with Fig. 8 reveals that this frequency dependence is substantially weaker than the effects of ultrasonic pressure amplitude. Notably, dual-oscillations of F_B within a single ultrasonic period vary inconsistently at different f_0. At 75 kHz, prominent high-frequency oscillations near zero amplitude emerge within each ultrasonic cycle.

Figure 13 presents the variation of F_B with N at different frequencies for bubbles with different initial radii. For all four tested pairs, the initial radius of bubble 1 (R_{10}) remains fixed at 20 μm. Significant differences in F_B characteristics emerge depending on both f_0 and specific bubble pairs. For example, when $R_{10} = 20$ μm and $R_{20} = 45$ μm, F_B exhibits four oscillations per ultrasonic cycle at $f_0 = 75$ kHz.

As evident from Fig. 13a and c, when $R_{20} = 45$ μm at $f_0 = 75$ kHz or when $R_{20} = 25$ μm at $f_0 = 125$ kHz, F_B alternates between attraction and repulsion within a single ultrasonic period. This behavior arises because the initial radii (45 and 25 μm) approach the resonance radii R_{res} for 75 and 125 kHz, respectively. Figure 13b and d

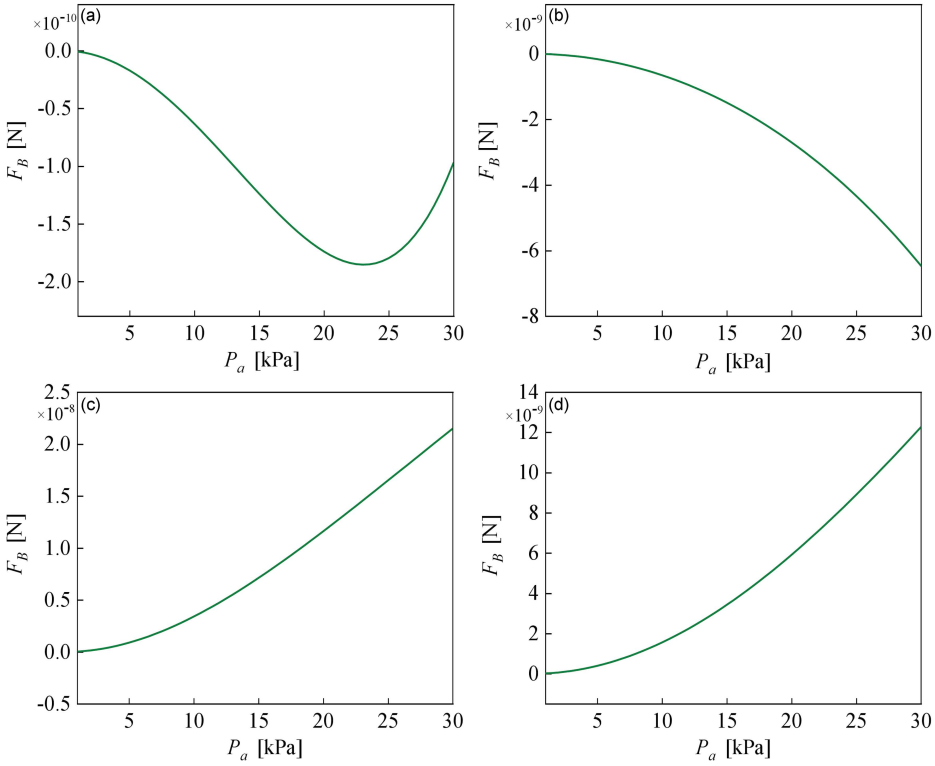

Fig. 10. Variations of F_B with ultrasonic pressure amplitude (P_a) for bubble pairs of different initial radii. Here, (a) $R_{10} = 20$ μm, $R_{20} = 15$ μm; (b) $R_{10} = 20$ μm, $R_{20} = 25$ μm; (c) $R_{10} = 20$ μm, $R_{20} = 35$ μm; (d) $R_{10} = 20$ μm, $R_{20} = 45$ μm. In all cases (a–d), $f_0 = 100$ kHz and $D_0 = 1000$ μm.

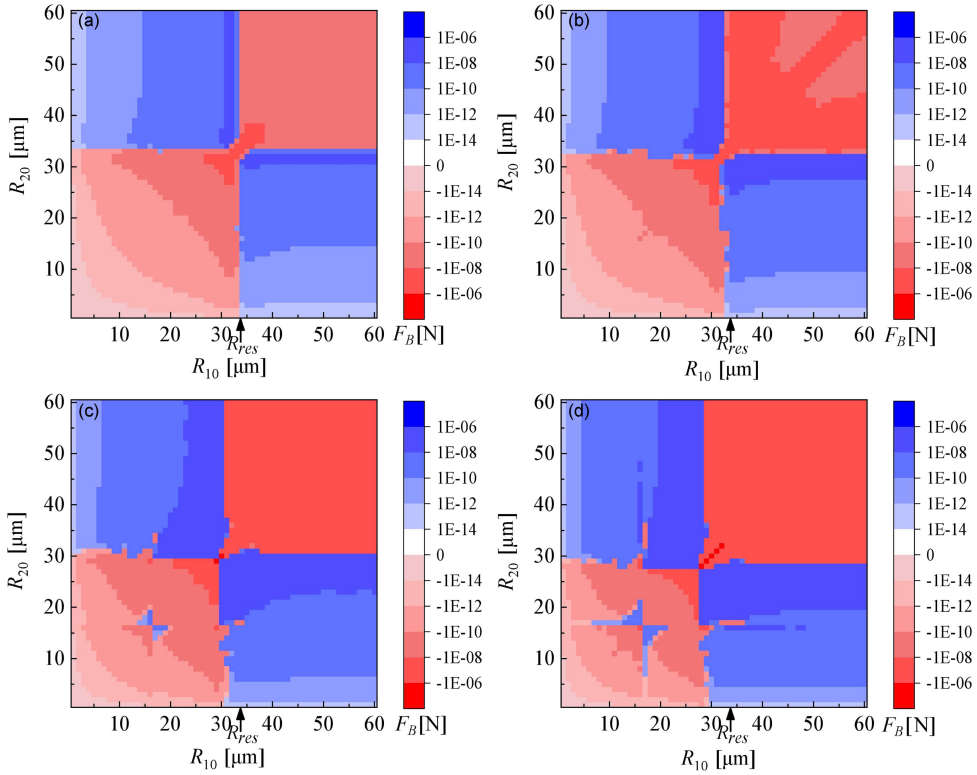

Fig. 11. Distributions of F_B in the R_{10}–R_{20} plane at different ultrasonic pressure amplitudes (P_a). Here, (a) $P_a = 5$ kPa; (b) $P_a = 10$ kPa; (c) $P_a = 20$ kPa; (d) $P_a = 30$ kPa. In all cases (a–d), $f_0 = 100$ kHz and $D_0 = 1000$ μm.

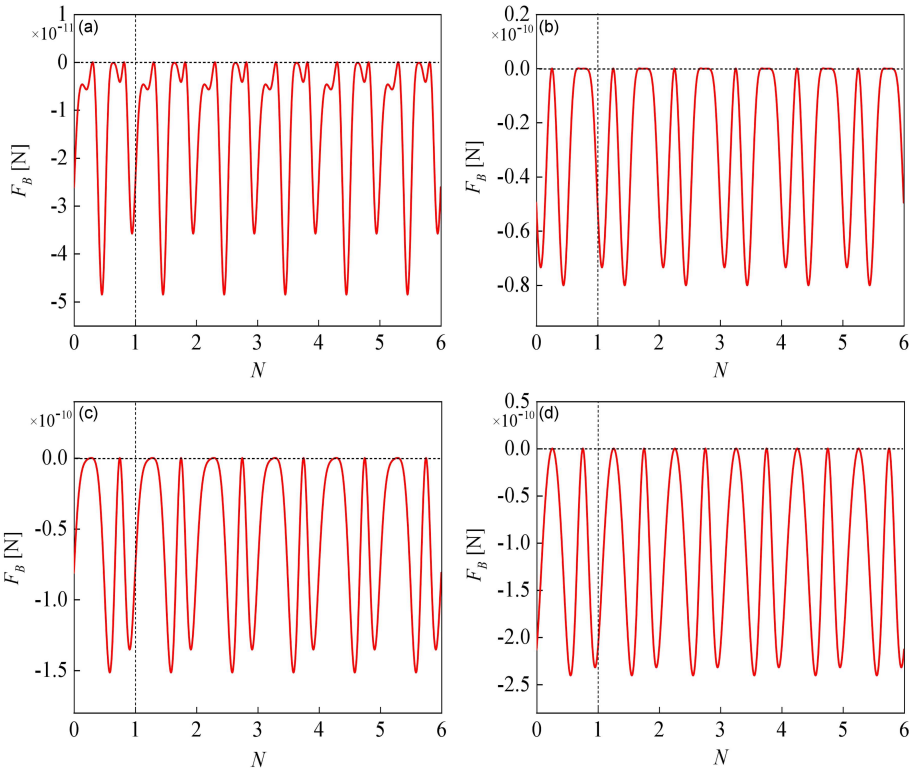

Fig. 12. Variations of F_B with the number of ultrasonic excitation periods (N) at different ultrasonic frequencies (f_0) for bubbles with the same initial radii. Here, (a) $f_0 = 75$ kHz; (b) $f_0 = 100$ kHz; (c) $f_0 = 125$ kHz; (d) $f_0 = 150$ kHz. In all cases (a–d), $P_a = 10$ kPa and $D_0 = 1000$ μm.

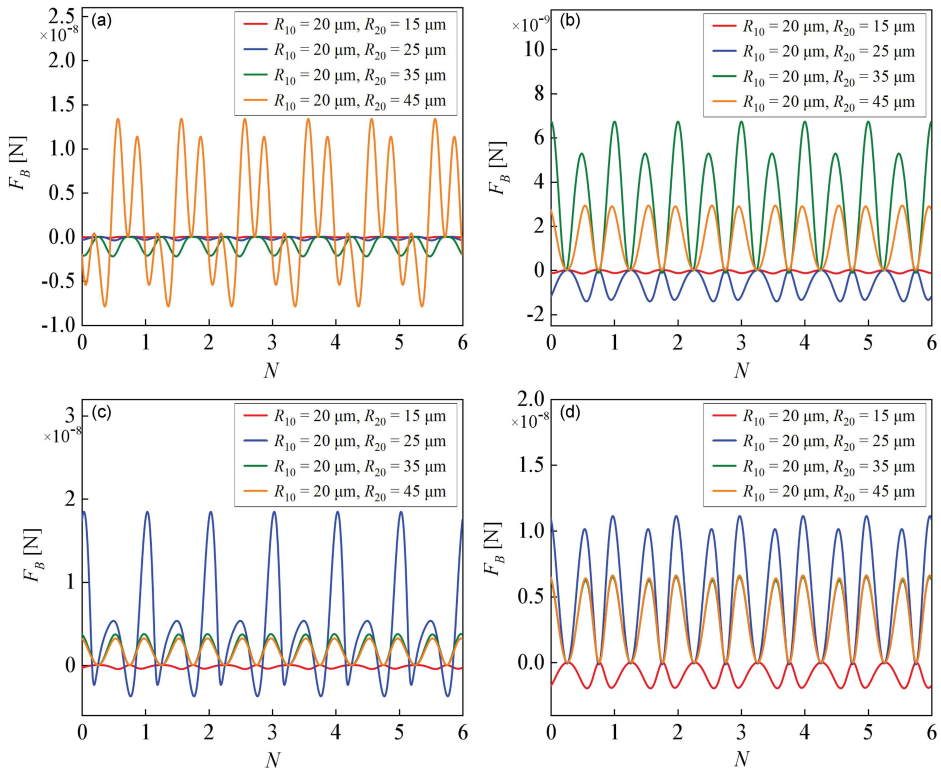

Fig. 13. Variations of F_B with the number of ultrasonic excitation periods (N) under different ultrasonic frequencies (f_0) for bubbles with different initial radii. Here, (a) $f_0 = 75$ kHz; (b) $f_0 = 100$ kHz; (c) $f_0 = 125$ kHz; (d) $f_0 = 150$ kHz. In all cases (a–d), $P_a = 10$ kPa, $D_0 = 1000$ μm.

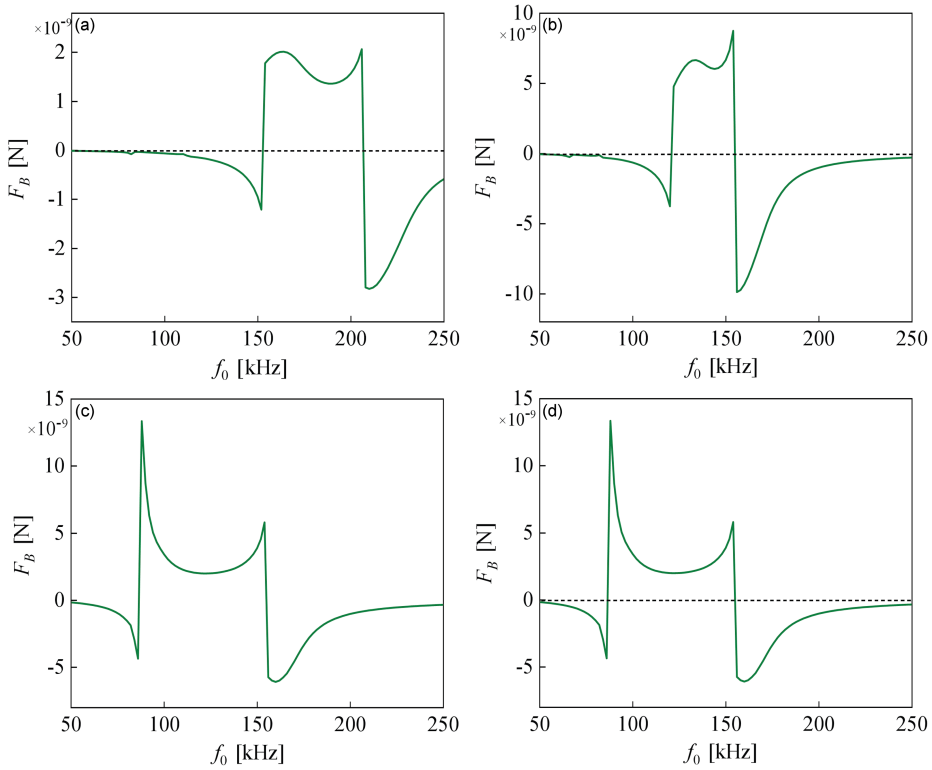

Fig. 14. Variations of F_B with ultrasonic frequency (f_0) for bubbles with different initial radii. Here, (a) $R_{10} = 20$ μm, $R_{20} = 15$ μm; (b) $R_{10} = 20$ μm, $R_{20} = 25$ μm; (c) $R_{10} = 20$ μm, $R_{20} = 35$ μm; (d) $R_{10} = 20$ μm, $R_{20} = 45$ μm. In all cases (a–b), $P_a = 10$ kPa and $D_0 = 1000$ μm.

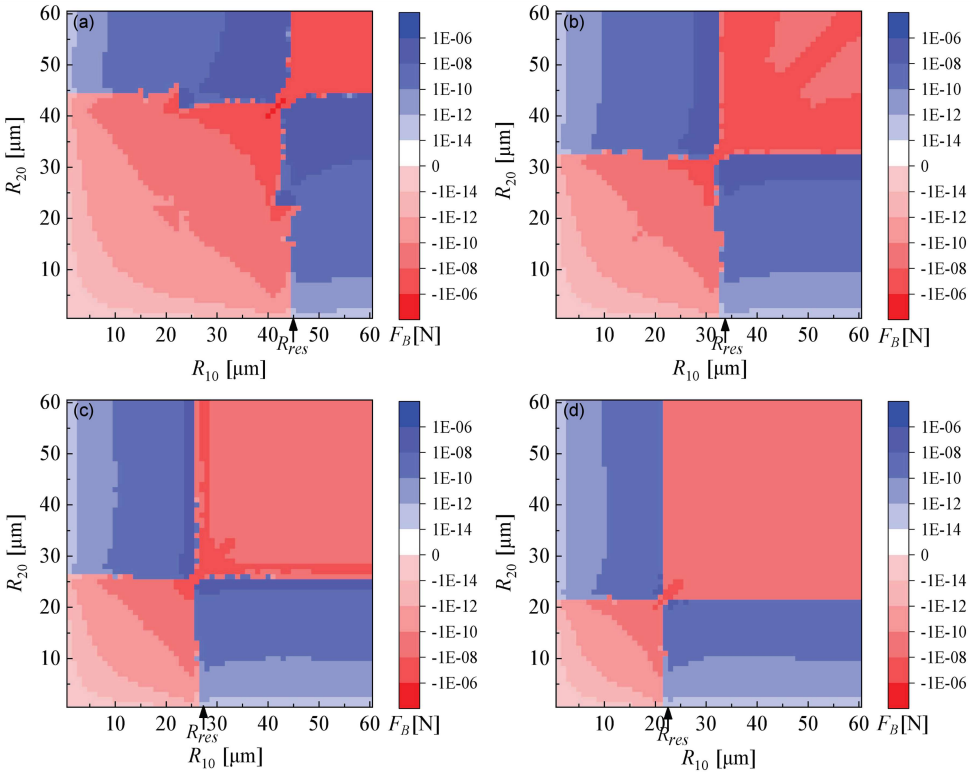

Fig. 15. Distributions of F_B in the R_{10}–R_{20} plane at different ultrasonic frequencies (f_0). Here, (a) $f_0 = 75$ kHz; (b) $f_0 = 100$ kHz; (c) $f_0 = 125$ kHz; (d) $f_0 = 150$ kHz. In all cases (a–d), $P_a = 10$ kPa and $D_0 = 1000$ μm.

show that when $R_{10} = 20$ μm and $R_{20} = 25$ μm, attraction occurs at 100 kHz, whereas repulsion dominates at 150 kHz. This behavior is clearly caused by the reversal of F_B.

In Fig. 14, the variation of time-averaged F_B as a function of f_0 for four different bubble pairs is illustrated. For each of the four bubble pairs, F_B undergoes two reversals as f_0 increases. These reversals occur when f_0 equals the linear resonance frequency (f_{res}) of either bubble within each bubble pair. The secondary Bjerknes force manifests attraction when the value of f_0 falls below the value of f_{res} of the larger bubble or exceeds that of the smaller bubble. Conversely, repulsion dominates when the value of f_0 lies between the values of f_{res} of the two bubbles. Additionally, the magnitude of F_B decays as f_0 moves away from f_{res} of either bubble.

Figure 15 illustrates the distribution of F_B in the R_{10}–R_{20} plane at different f_0. The results demonstrate that as f_0 increases, the linear resonance radius R_{res} decreases, shifting the attraction–repulsion boundary toward smaller bubble radii. Furthermore, near the boundary, the absolute value of F_B decreases as f_0 increases. The absence of additional reversals of F_B is attributed to amplitude-limited subharmonic/harmonic resonances of bubbles under low ultrasonic pressure ($P_a = 10$ kPa).

4. Conclusions

This study utilizes ultrasound-induced secondary Bjerknes forces (F_B) and associated dynamical models to investigate the dependence of F_B on initial radii (R_{10}, R_{20}), inter-bubble distance (D_0), and ultrasonic excitation parameters (P_a, f_0).

The distribution of F_B in the R_{10}–R_{20} plane is divided into four distinct regimes, i.e., attractive-dominant zones, where ($R_{10} < R_{res}$ and $R_{20} < R_{res}$) or ($R_{10} > R_{res}$ and $R_{20} > R_{res}$), and repulsive-dominant zones, where ($R_{10} < R_{res}$ and $R_{20} < R_{res}$) or ($R_{10} > R_{res}$ and $R_{20} > R_{res}$). Maximum inter-bubble forces occur when both radii approach the linear resonance radius (R_{res}). The distribution profile of F_B in the R_{10}–R_{20} space remains fundamentally invariant across varying D_0. Moreover, the magnitude of F_B exhibits inverse scaling with D_0, and the transition boundary between attractive and repulsive zones migrates toward larger initial radii as D_0 decreases.

The secondary Bjerknes force increases with increasing P_a. Crucially, P_a directly affects the temporal characteristics of F_B within an acoustic cycle. Higher P_a further shifts the attractive–repulsive phase boundary toward smaller initial bubble radii. The ultrasonic frequency (f_0) exerts a weaker influence on F_B than P_a. Across tested bubble radii, F_B undergoes two reversals with increasing f_0, while the attractive-repulsive boundary migrates toward smaller radii under elevated-frequency conditions.

Acknowledgments

This study was supported by the BPU Key Program (grant No. 2024X019-KXZ).

Appendix

The computation code utilized in this work was developed as MATLAB scripts [32]

Fun program

```
function dydt = fun(t,y,R10,R20)
 global c L rho P0 sigma k mu pi f1 f2 g1 g2 Pv
  P1 P2;
 dydt = zeros(4,1);
 A1 = (1-y(2)/c)*y(1)+4*mu/rho/c;
 B1 = 1.5*(1-y(2)/3/c)*(y(2)^2)
 +2/L*y(3)*(y(4)^2)-1/rho*(1+y(2)/c)
 *((P0-Pv+2*sigma/R10)*((R10/y(1))^(3*k))
 -P0+Pv-2*sigma/y(1)-4*mu*y(2)/y(1)
 -P1*sin(2*pi*f1*t+g1)-P2*sin(2*pi*f2*t+g2))
 +3*k*y(2)/rho/c*(P0-Pv+2*sigma/R10)
 *((R10/y(1))^(3*k))
 -2*sigma*y(2)/rho/c/y(1)
 -4*mu*(y(2)^2)/rho/c/y(1)
 +y(1)*2*pi*f1*P1/rho/c*cos(2*pi*f1*t+g1)
 +y(1)*2*pi*f2*P2/rho/c*cos(2*pi*f2*t+g2);
 C1 = 1/L*(y(3)^2);
 A2 = (1-y(4)/c)*y(3)+4*mu/rho/c;
 B2 = 1.5*(1-y(4)/3/c)*(y(4)^2)
 +2/L*y(1)*(y(2)^2)-1/rho*(1+y(4)/c)
 *((P0-Pv+2*sigma/R20)*((R20/y(3))^(3*k))
 -P0+Pv-2*sigma/y(3)-4*mu*y(4)/y(3)
 -P1*sin(2*pi*f1*t+g1)-P2*sin(2*pi*f2*t+g2))
 +3*k*y(4)/rho/c*(P0-Pv+2*sigma/R20)
 *((R20/y(3))^(3*k))
 -2*sigma*y(4)/rho/c/y(3)
 -4*mu*(y(4)^2)/rho/c/y(3)
 +y(3)*2*pi*f1*P1/rho/c*cos(2*pi*f1*t+g1)
 +y(3)*2*pi*f2*P2/rho/c*cos(2*pi*f2*t+g2);
 C2 = 1/L*(y(1)^2);
 dydt(1) = y(2);
 dydt(2) = (C1*B2-A2*B1)/(A1*A2-C1*C2);
 dydt(3) = y(4);
 dydt(4) = (C2*B1-A1*B2)/(A1*A2-C1*C2);
end
```

Main program

```
clear;
clc;
global c L rho P0 Pv sigma k mu pi f1 f2 g1 g2
P1 P2;
pi = 3.14159;
```

```
f1 = 100*10^3;
f2 = 200*10^3;
g1 = 0;
g2 = 0;
L = 1000*10^(-6);
P0 = 1*10^5;
P1 = -2150;
P2 = -2150;
Pv = 2330;
k = 1.4;
rho = 1000;
sigma = 0.0725;
mu = 0.001;
c = 1500;
time = 1./f1;
step = time/500;
ttime = 50*time;
bf1 = 100;
bf2 = 100;
R10 = linspace(10e-6,50e-6,bf1);
R20 = linspace(10e-6,50e-6,bf2);
fb = zeros(bf2,bf1);
for m = 1:bf1
 for i = 1:bf2
  y0 = [R10(m);0;R20(i);0];
  options = odeset('RelTol',1e-9);
  [t,y] = ode45(@fun,(0:step:ttime),y0,options,
  R10(m),R20(i));
  N = numel(t);
  for j = N-500:N-1
   fb(i,m) = fb(i,m)+(4*pi*rho)
   *((y(j,1)^2)*(y(j,3)^2)*y(j,2)*y(j,4)
   +(y(j+1,1)^2)*(y(j+1,3)^2)*y(j+1,2)
   *y(j+1,4))*step/2/time;
  end
 end
end
figure;
imagesc(R10,R20,fb);
set(gca,'ydir','normal');
axis equal tight;
```

References

[1] Y. Xuan, T. Liu, L. Nastac, L. Brewer, I. Levin, V. Arvikar, *Metall. Mater. Trans. A* **49**, 3346 (2018).

[2] S.G. Yunusov, N.K. Andryushchenko, A.Z. Aliyeva, S.M. Aleskerova, *Processes Petroch. Oil Refin.* **25**, 98 (2024).

[3] C. Liu, Q. Xu, J. Ma, S. Wang, J. Li, X. Mao, *Ultras. Sonochem.* **103**, 106771 (2024).

[4] E.R. Trumble, J.H. Huang, *Oper. Neurosurg.* **24**, e471 (2023).

[5] C. Lei, B. Jacobson, J.M. Hartley, S. Scott, I. Sumarlan, A. Feeney, P. Prentice, K.S. Ryder, A.P. Abbott, *Ultrason. Sonochem.* **110**, 107049 (2024).

[6] A. Salaeh, *Arch. Acoust.* **49**, 439 (2024).

[7] X. Wu, *Ultrasound Obstet. Gynecol.* **64**, 324 (2024).

[8] F. Yang, W. Dou, H. Wang, D. Cui, C. Li, *Medicine* **102**, e35535 (2023).

[9] V. Sokolenko, W. Elsner, A. Dróżdż, R. Gnatowska, *Acta Phys. Pol. A* **139**, 613 (2021).

[10] B. Lixin, W. Pengfei, L. Huiyu, Y. Jiuchun, S. Chang, L. Chao, *Ultrason. Sonochem.* **44**, 184 (2018).

[11] C. Wang, T. Connolley, I. Tzanakis, D. Eskin, J. Mi, *Materials* **13**, 44 (2020).

[12] N. Vyas, M. Mahmud, Q.X. Wang, A.D. Walmsley, *J. Vis. Exp.* **163**, e61509 (2020).

[13] V.F.K. Bjerknes, *Fields of Force: A Course of Lectures in Mathematical Physics Delivered December 1 to 23, 1905*, Columbia University Press (Macmillan), New York 1906.

[14] L.A. Crum, *J. Acoust. Soc. Am.* **57**, 1363 (1975).

[15] R. Mettin, I. Akhatov, U. Parlitz, C.D. Ohl, W. Lauterborn, *Phys. Rev. E* **56**, 2924 (1997).

[16] Y. Zhang, Q. Min, Y. Zhang, X. Du, *J. Hydrodyn.* **28**, 832 (2016).

[17] X. Wang, Z. Ning, M. Lv, J. Yao, C. Sun, *J. Phys. Soc. Jpn.* **91**, 014401 (2022).

[18] J. Liu, X. Wang, J. Liang, Y. Qiao, *Ultrason. Sonochem.* **102**, 106756 (2024).

[19] H. Chen, Z. Lai, Z. Chen, Y. Li, *Ultrason. Sonochem.* **52**, 344 (2019).

[20] J. Jiao, Y. He, S.E. Kentish, M. Ashokkumar, R. Manasseh, J. Lee, *Ultrasonics* **58**, 35 (2015).

[21] A.A. Doinikov, T. Combriat, P. Thibault, P. Marmottant, *Phys. Rev. E* **94**, 023105 (2016).

[22] Y. Zhang, Y. Zhang, S. Li, *Ultrason. Sonochem.* **29**, 129 (2016).

[23] H. Chen, Z. Chen, Y. Li, *Ultrason. Sonochem.* **61**, 104814 (2020).

[24] Y. Wang, D. Chen, P. Wu, J. Li, *Phys. Fluids* **36**, 046109 (2024).

[25] Q. Zou, X. Zhong, B. Zhang, A. Gao, X. Wang, Z. Li, D. Qin, *Ultrasonics* **134**, 107089 (2023).

[26] Y. Shen, L. Zhang, Y. Wu, W. Chen, *Ultrason. Sonochem.* **73**, 105535 (2021).

[27] X. Wang, Z. Ning, M. Lv, X. Wang, C. Hu, *Acta Phys. Pol. A* **148**, 99 (2025).

[28] G. Regnault, A.A. Doinikov, C. Mauger, P. Blanc-Benon, C. Inserra, *Phys. Fluids* **35**, 037116 (2023).

[29] P. Fan, D. Yang, J. Wu, Y. Yang, X. Guo, J. Tu, D. Zhang, *Ultrason. Sonochem.* **53**, 178 (2019).

[30] L. Meng, X. Liu, Y. Wang et al. *Adv. Sci.* **6**, 1900557 (2019).

[31] D. Qin, S. Lei, B. Zhang, Y. Liu, J. Tian, X. Ji, H. Yang, *Ultrason. Sonochem.* **104**, 106808 (2024).

[32] X. Wang, Data Analysis Tool, Github, 2025.

[33] X. Wang, Z. Ning, M. Lv, P. Wu, C. Sun, Y. Liu, *Ultrason. Sonochem.* **92**, 106271 (2023).

[34] R.I. Nigmatulin, I.S. Akhatov, N.K. Vakhitova, R.T. Lahey, *J. Fluid Mech.* **414**, 47 (2000).

[35] A.A. Doinikov, *Phys. Rev. E* **64**, 026301 (2001).

[36] V.G. Levich, in: *Physicochemical Hydrodynamics*, Prentice-Hall, Englewood Cliffs (NJ) 1962, p. 46.

[37] W. Lauterborn, T. Kurz, *Rep. Prog. Phys.* **73**, 106501 (2010).

[38] L. Zhang, W. Chen, Y. Wu, Y. Shen, G.-Y. Zhao, *Chinese Phys. B* **30**, 104301 (2021).